Supporting Information for:

In Situ Formed Nickel Phosphide/Iron Oxide Heterojunction for Accelerating Hydrogen Generation

Wenjing Xu,*[a] Wei Li,[a] Wei Chen,[b] Mei Liu,[a] Xianji Guo[c] and Baojun Li*[c]

[a] School of Science, Jiaozuo Normal College, Jiaozuo, Henan 454000, PR China

[b] Jiaozuo Houji Chemical Co., LTD, Jiaozuo, Henan 454500, PR China

[c] College of Chemistry, Zhengzhou University, Zhengzhou 450001, PR China

* Corresponding Author. xwj900128@jzsz.edu.cn (W J Xu), lbjfcl@zzu.edu.cn (B J Li).

Total number of pages: 26

Total number of Figures: 22

Total number of Tables: 5

Experimental Section

Chemicals. Ferric nitrate nonahydrate (Fe(NO$_3$)$_3$·9H$_2$O), nickel nitrate hexahydrate (Ni(NO$_3$)$_2$·6H$_2$O), glycerol, isopropanol and sodium hypophosphite (NaH$_2$PO$_2$) were purchased from Sinopharm Chemical Reagent Co., Ltd. (Shanghai, China). Ammonia borane (NH$_3$BH$_3$), sodium hydroxide (NaOH), and ethanol were supplied by Maclin Biochemical Technology Co., Ltd (Shanghai, China). All reagents used in this study are analytical grade.

Characterization. The micro morphologies of the samples were characterized using JSM-6700F scanning electron microscopy (SEM, JEOL Ltd., Japan). The specific surface areas of the samples were measured with nitrogen adsorption isotherms on a specific surface analyzer (ASAP 2420, Micrometrics, USA). The Brunauer-Emmett-Teller (BET) and nonlocalization density functional theory (NLDFT) techniques were employed for surface area and pore diameter calculation. The thermogravimetric analysis (TGA) experiments were carried out on a STA 449F3 thermal analyzer (Netzsch, Germany) in argon flow under temperature range from 30 °C to 800 °C at 10 °C min^{-1}.

Catalytic hydrolysis of NH$_3$BH$_3$. Catalytic performance of as-prepared catalysts was evaluated through a water-displacement method to collect the generated hydrogen during the NH$_3$BH$_3$ hydrolysis. The catalyst (15 mg) was put into a round bottom flask (50 mL) fixed on an electric heated thermostatic magnetic stirring water bath. Then, a NH$_3$BH$_3$ aqueous solution (5 mL, 0.246 mol L^{-1}) containing NaOH (200 mg, 1.0 mol L^{-1}) was injected through a syringe. The reaction was carried out under magnetic stirring at 500 rpm, 25 °C. The produced hydrogen flowed into a gas burette (100 mL) filled with water, and the volume of water was equal to the volume of hydrogen produced. The specific rates (r_B) of hydrogen generation were calculated as follows (eq. 1):

$$r_B = \frac{40(mL)}{[t_{60} - t_{20}] \cdot w_c(g)} \qquad \text{(eq. 1)}$$

Where t_{60} and t_{20} represent the time for 60 and 20 mL of hydrogen generation, respectively, and w_c is the weight of Ni in the catalyst.

The value of turnover frequency (TOF, min^{-1}), which is used to evaluate the catalytic activity of catalyst in NH$_3$BH$_3$ hydrolysis, was calculated by the following equation:

$$\text{TOF} = \frac{n_{H_2}}{n_{Ni}t} \qquad \text{(eq. 2)}$$

Where n_{H2} is the moles of H_2 generated and t is the reaction time during the 20-60 mL. n_{Ni} is the total moles of Ni in the catalysts. Due to the monometallic catalyst of $Ni_2P@C$ displays much higher activity than $P\text{-}Fe_3O_4@C$ and the catalytic activity of $P\text{-}Fe_3O_4@C$ is extremely low, r_B and TOF values are calculated according to the nickel content.

Computational Method

We employed the first-principles [1,2] to perform all density functional theory (DFT) calculations within the generalized gradient approximation (GGA) using the Perdew-Burke-Ernzerhof (PBE) [3] formulation. We chose the projected augmented wave (PAW) potentials [4,5] to describe the ionic cores and take valence electrons into account using a plane wave basis set with a kinetic energy cutoff of 520 eV. Partial occupancies of the Kohn-Sham orbitals were allowed using the Gaussian smearing method and a width of 0.05 eV. The electronic energy was considered self-consistent when the energy change was smaller than 10^{-6} eV. A geometry optimization was considered convergent when the energy change was smaller than 0.05 eV $Å^{-1}$. The vacuum spacing in a direction perpendicular to the plane of the structure was 20 Å for the surfaces. The Brillouin zone integration was performed using $2 \times 2 \times 1$ Monkhorst-Pack k-point sampling for a structure. Finally, the adsorption energies (E_{ads}) were calculated as $E_{ads} = E_{ad/sub} - E_{ad} - E_{sub}$, where $E_{ad/sub}$, E_{ad}, and E_{sub} are the total energies of the optimized adsorbate/substrate system, the adsorbate in the structure, and the clean substrate, respectively. The free energy was calculated using the equation:

$G = E_{ads} + E_{ZPE} - TS$

where G, E_{ads}, E_{ZPE} and TS are the free energy, total energy from DFT calculations, zero point energy and entropic contributions, respectively.

Table S1. Pyrolysis conditions and the contents of Fe and Ni determined by ICP-MS.

Sample	Precursor	Pyrolysis conditions	Fe[a] (wt%)	Ni[a] (wt%)	n_{Fe}/n_{Ni}	TOF (min^{-1})
$Fe_3O_4-Ni_2P@C$	FeNi-Gly	NaH_2PO_2, N_2, 300 °C, 4 h	6.35	14.21	1/2.13	92.8
P-FeNiO$_x$@C-250	FeNi-Gly	NaH_2PO_2, N_2, 250 °C, 4 h	6.75	15.25	1/2.13	50.3
$Fe_3O_4-Ni_2P@C$-400	FeNi-Gly	NaH_2PO_2, N_2, 400 °C, 4 h	6.41	14.44	1/2.13	32.3
$Fe_3O_4-Ni_2P@C$-600	FeNi-Gly	NaH_2PO_2, N_2, 600 °C, 4 h	6.84	15.32	1/2.13	14.5
$Ni_2P@C$	Ni-Gly	NaH_2PO_2, N_2, 300 °C, 4 h	0	23.01	0/1	20.0
P-Fe_3O_4@C	Fe-Gly	NaH_2PO_2, N_2, 300 °C, 4 h	22.12	0	1/0	\
Fe_3O_4-NiO@C	FeNi-Gly	N_2, 300 °C, 4 h	11.30	25.31	1/2.13	7.3

[a] Measured by inductively coupled plasma mass spectrometry (ICP-MS, PQ-MS, Germany).

Table S2. Element contents of samples from XPS.

Samples	Atomic ratio (at.%)				
	P 2p	C 1s	O 1s	Fe 2p	Ni 2p
$Fe_3O_4-Ni_2P@C$	18.20	15.63	58.55	3.86	3.76
P-FeNiO$_x$@C-250	12.24	18.46	57.70	3.96	7.64
$Fe_3O_4-Ni_2P@C$-400	18.45	17.93	54.69	3.54	5.39
$Fe_3O_4-Ni_2P@C$-600	15.90	26.29	48.95	4.88	3.98
$Ni_2P@C$	16.36	17.74	56.49	0	9.41
P-Fe_3O_4@C	15.01	16.75	54.69	13.55	0
Fe_3O_4-NiO@C	0	30.09	50.34	6.09	13.48

Table S3. Textural properties obtained from N_2-adsorption isotherms analysis.

Sample	BET surface area ($m^2 g^{-1}$)	Total pore volume ($cm^3 g^{-1}$)	Average pore width (nm)
Fe_3O_4-$Ni_2P@C$	72.9	0.25	13.0

Table S4. TOF values reported in the literatures.

Catalysts	TOF (H_2) (min^{-1})	T (°C)	Ref.
Fe_3O_4-$Ni_2P@C$	92.8	25	This work
Ni/ZIF-8	85.7	25	6
$Cu@Ni_6$-MOF	69.1	25	7
NiMn-decorated CNFs	58.2	30	8
$Cu_{0.5}Ni_{0.5}$/CMK-1	54.8	25	9
Ni NPs@3D-(N)GFs	41.7	25	10
Ni_2P	40.4	25	11
Ni@MCS-30	30.7	25	12
Ni/CNT	26.2	25	13
Ni NPs/CNT	23.5	25	14
$Ni_{12}P_5$	23.0	25	15
hcp-CuNi/C	22.64	25	16
hcp-Ni/C	4.32	25	16
fcc-Ni/C	2.10	25	16
Ni@ZIF-8	14.2	25	17
$Cr_2Ni_3@carbon$	5.78	25	18
Ni/AC	4.8	25	19

Table S5. The free energy changes at different simulated catalysts by DFT calculations.

Catalysts	Physical adsorption state energy (eV)		Transition state energy (eV)		Reaction barrier (eV)	
	NH_3BH_3	H_2O	NH_3BH_3	H_2O	NH_3BH_3	H_2O
$Fe_3O_4@C$	-0.258	-0.105	1.972	0.729	2.230	0.834
$Ni_2P@C$	-0.392	-0.203	1.592	0.413	1.984	0.616
Fe_3O_4-$Ni_2P@C$	-0.726	-0.317	-0.279	0.103	0.447	0.420
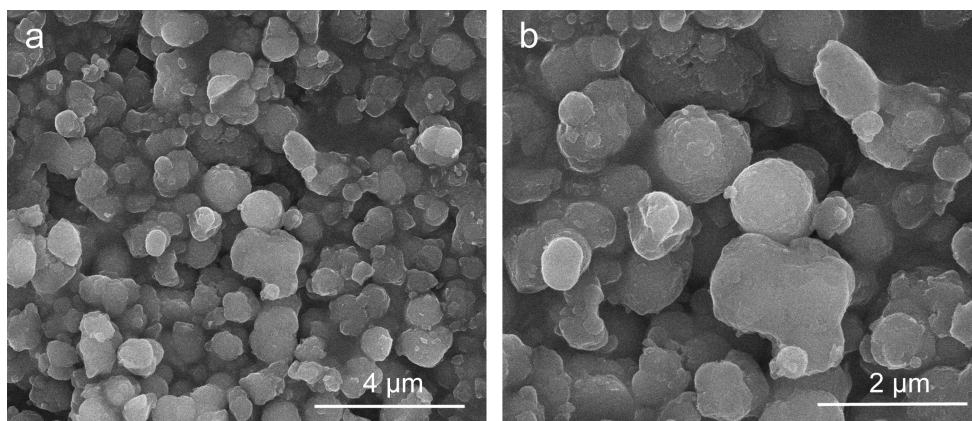
Fig. S1. (a, b) SEM images of FeNi-Gly.
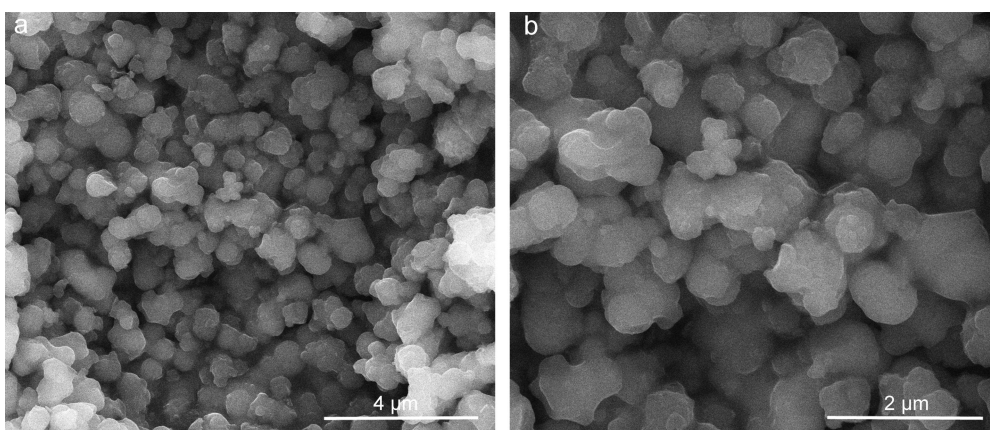
Fig. S2. (a, b) SEM images of Fe_3O_4-$Ni_2P@C$.
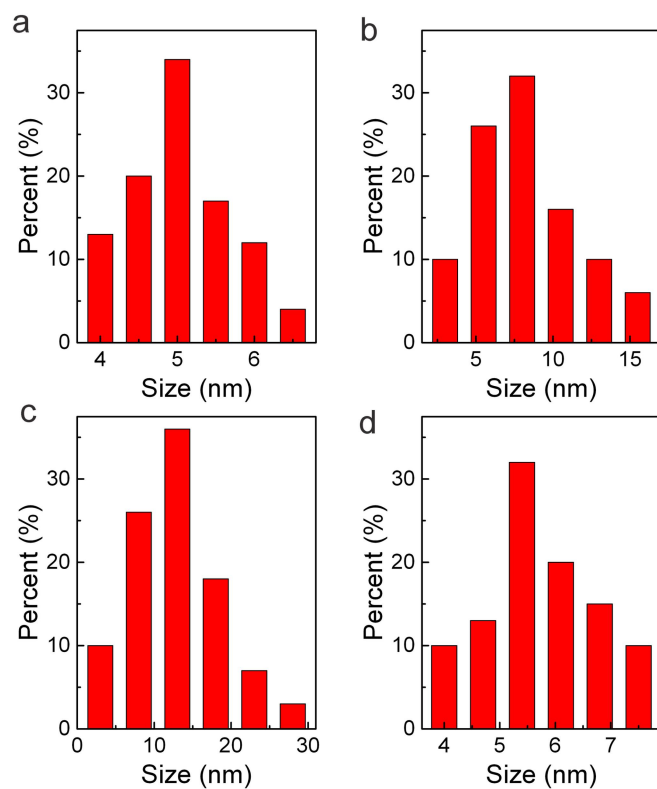
Fig. S3. Particle size distribution curves of (a) Fe_3O_4-Ni_2P in the Fe_3O_4-$Ni_2P@C$ catalyst, (b) Fe_3O_4-Ni_2P in the Fe_3O_4-$Ni_2P@C$-600 catalyst, (c) Ni_2P in the $Ni_2P@C$ catalyst, and (d) Fe_3O_4-NiO in the Fe_3O_4-NiO@C catalyst.
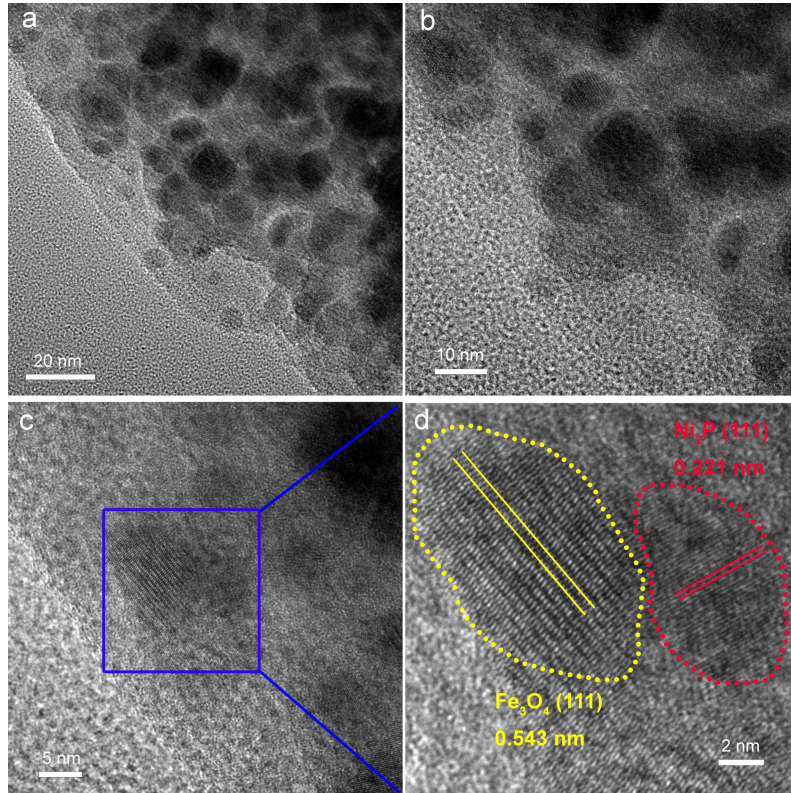
**Fig. S4.** TEM and HRTEM images of Fe_3O_4-Ni_2P@C-600.
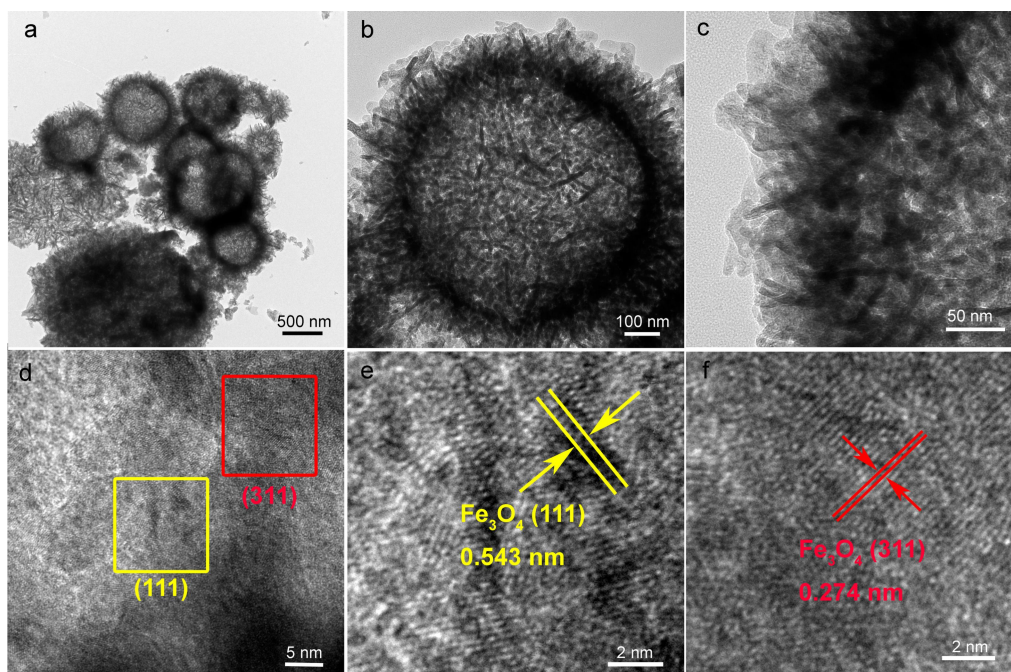
Fig. S5. TEM and HRTEM images of P-Fe₃O₄@C. TEM images of P-Fe₃O₄@C displays a hollow sphere morphology with diameters of about 500 nm, and the lattice spacing of about 0.543 and 0.274 nm, corresponding to (111) and (311) crystal planes of cubic Fe₃O₄, respectively, are observed in the HRTEM images.
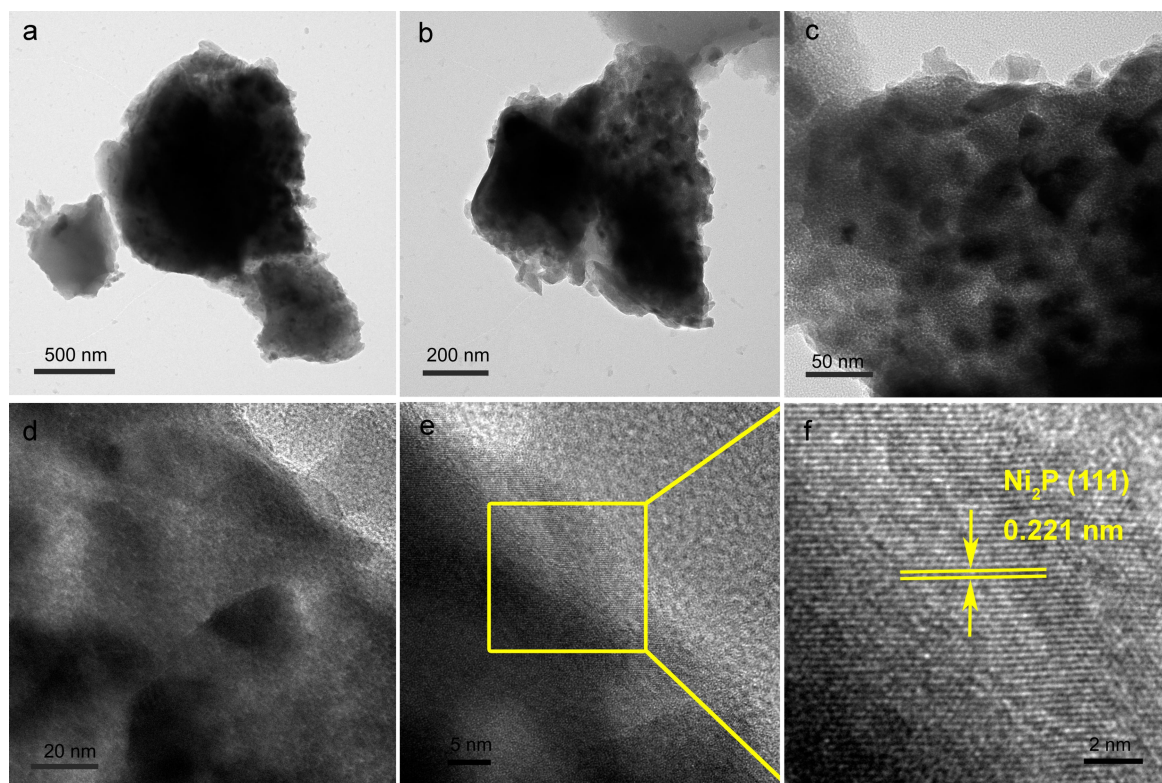
Fig. S6. TEM and HRTEM images of Ni$_2$P@C. Large amounts of Ni$_2$P nanocrystals distribute in the amorphous carbon support and the lattice plane of Ni$_2$P (111) is found in the HRTEM image of Ni$_2$P@C.
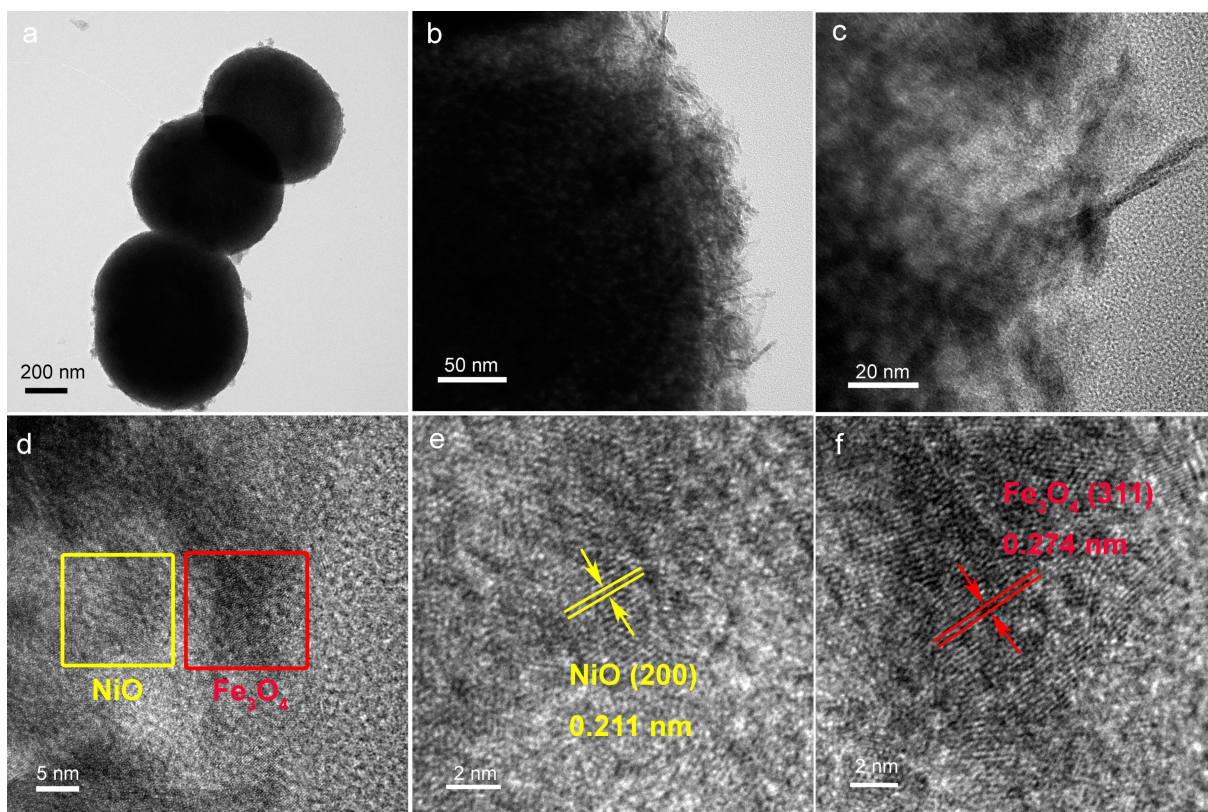
Fig. S7. TEM and HRTEM images of Fe_3O_4-NiO@C. Fe_3O_4-NiO@C sample was synthesized under the same conditions of Fe_3O_4-Ni_2P@C except for the absence of NaH_2PO_2. TEM images of Fe_3O_4-NiO@C exhibit a spherical morphology with diameters of about 600 nm. The lattice spacing of approximately 0.211 and 0.274 nm coincide well with the NiO (200) [20,21] and Fe_3O_4 (311) planes, respectively.
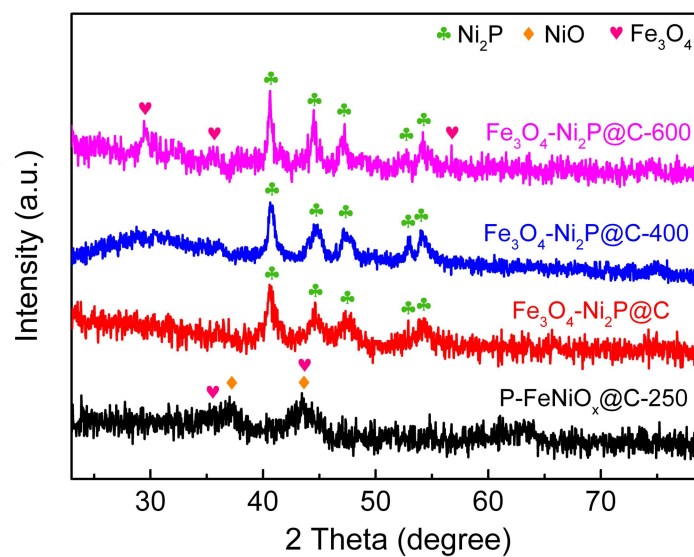
Fig. S8. PXRD patterns of the samples prepared at different phosphorization temperatures. Fe_3O_4-$Ni_2P@C$-600 and Fe_3O_4-$Ni_2P@C$-400 exhibit higher peak intensity than Fe_3O_4-$Ni_2P@C$, and the characteristic peaks of Fe_3O_4 are also observed in the Fe_3O_4-$Ni_2P@C$-600, suggesting their larger crystal grains due to the higher pyrolysis temperature. P-$FeNiO_x@C$-250 sample consists of NiO and Fe_3O_4 crystals without Ni_2P.
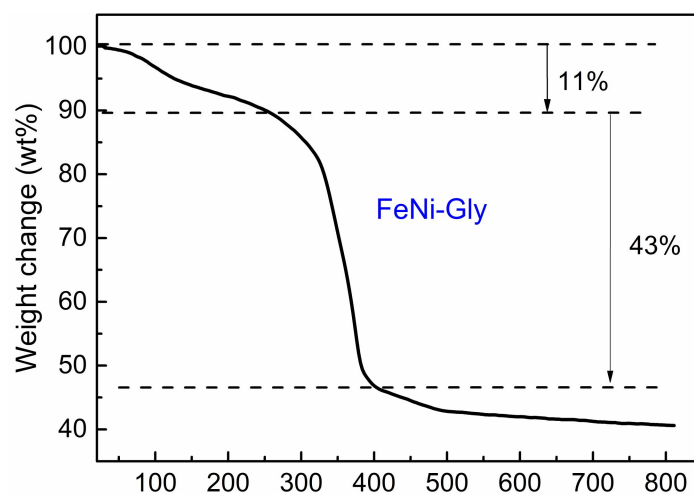
Fig. S9. The TGA curve of FeNi-Gly. The TGA result of FeNi-Gly in argon flow displays two mass losses. The first mass loss of 11.0 wt% occurred between 30 and 260 °C, due to the loss of adsorbed water molecules. The second mass loss of 43.0 wt% within 260-404 °C could be attributed to the decomposition of glycerol ligand in FeNi-Gly [22]. FeNi-Gly rarely decomposes in argon flow at 300 °C.
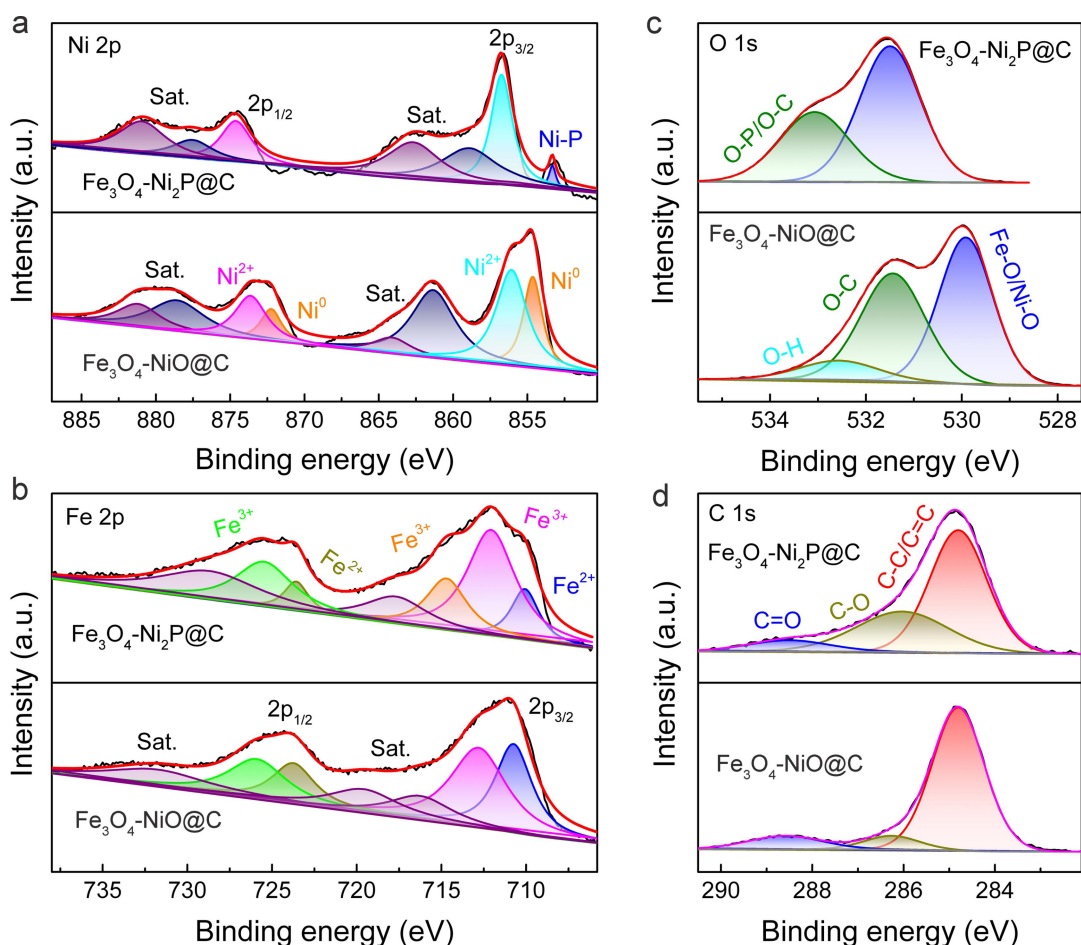
Fig. S10. (a-d) XPS spectra of Ni 2p, Fe 2p, O 1s and C 1s of the Fe_3O_4-$Ni_2P@C$ and Fe_3O_4-$NiO@C$ catalysts. Fig. S10a suggests that nickel element is mainly present in Ni^0 (854.7 and 872.2 eV), and Ni^{2+} oxidation state (856.1 and 873.7 eV) in the Fe_3O_4-$NiO@C$, while mainly in Ni^{2+} (856.7 and 874.6 eV) in the Fe_3O_4-$Ni_2P@C$. Fig. S10b shows iron element is in Fe^{2+} (710.1-710.8 eV) and Fe^{3+} (712.0-714.7 eV) in the two catalysts. The peak of Ni^0 2p completely disappeared during surface-phosphorization process, suggesting that P species reacted with Ni^0 and was introduced into the material successfully. Compared to Fe_3O_4-$NiO@C$ catalyst, the binding energies of Ni 2p, Fe 2p and O 1s shift after the formation of Fe_3O_4-$Ni_2P@C$ catalyst, indicating intrinsic charge redistribution among these elements during introducing P. This fact provides solid evidence of the role of phosphorization.
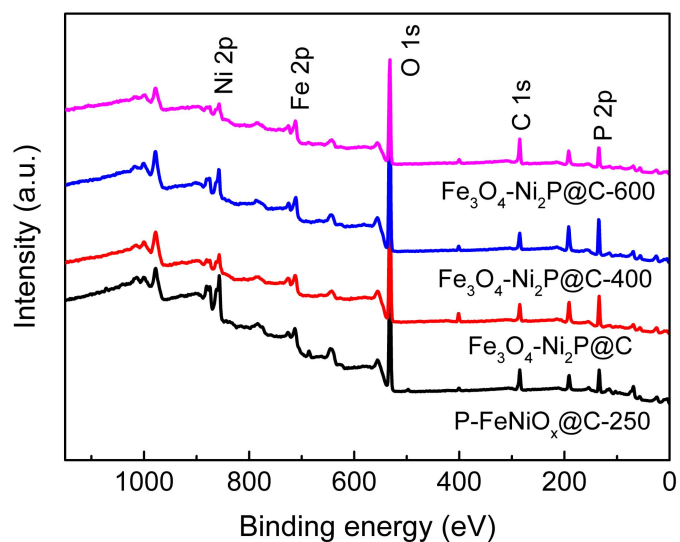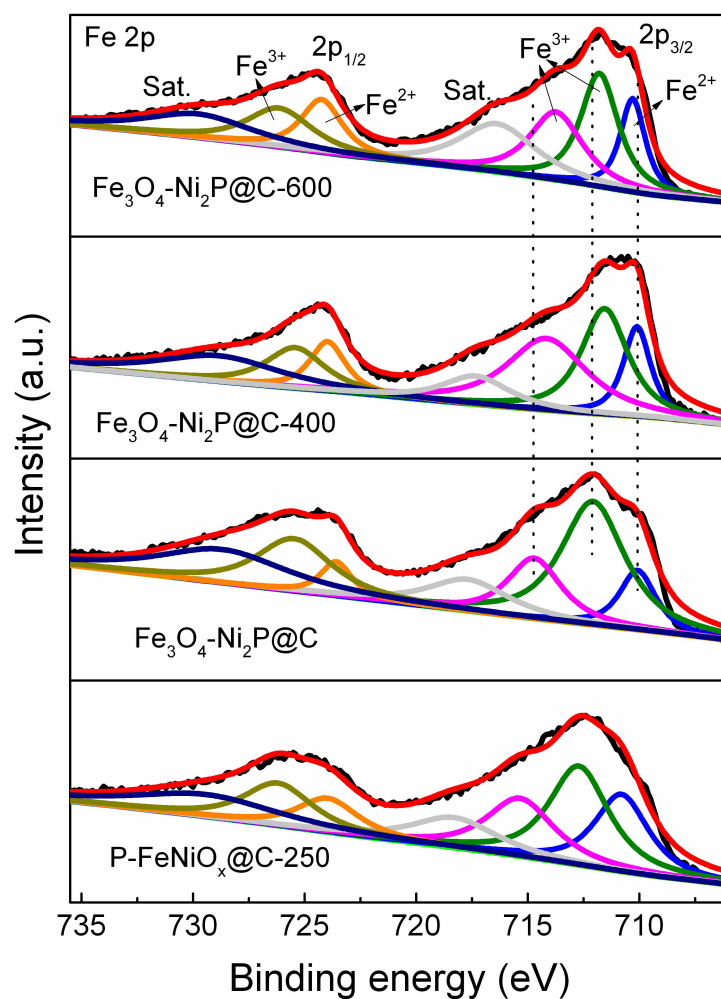
Fig. S11. The survey XPS spectra of samples prepared at different temperatures. The image clearly shows the presence of Fe, Ni, C, O, and P elements, indicating successful synthesis of samples at different temperatures.
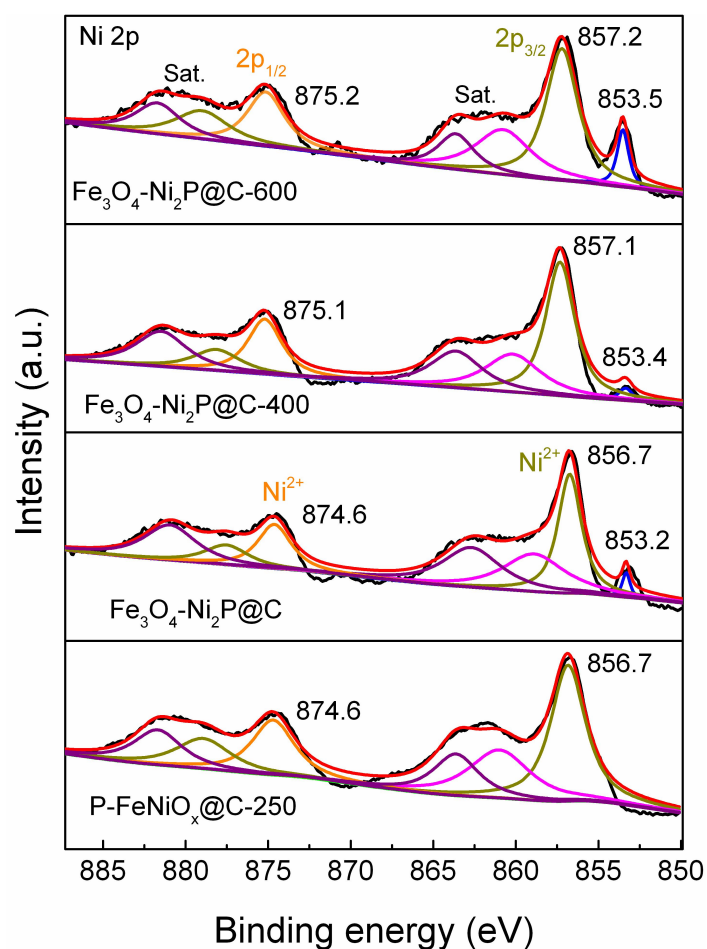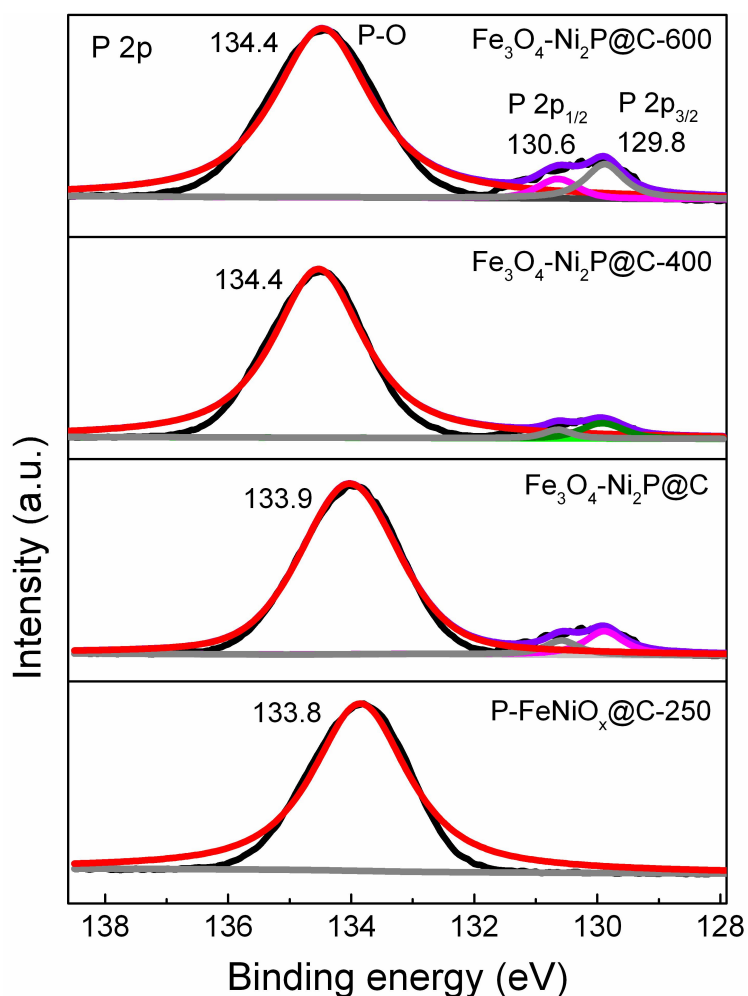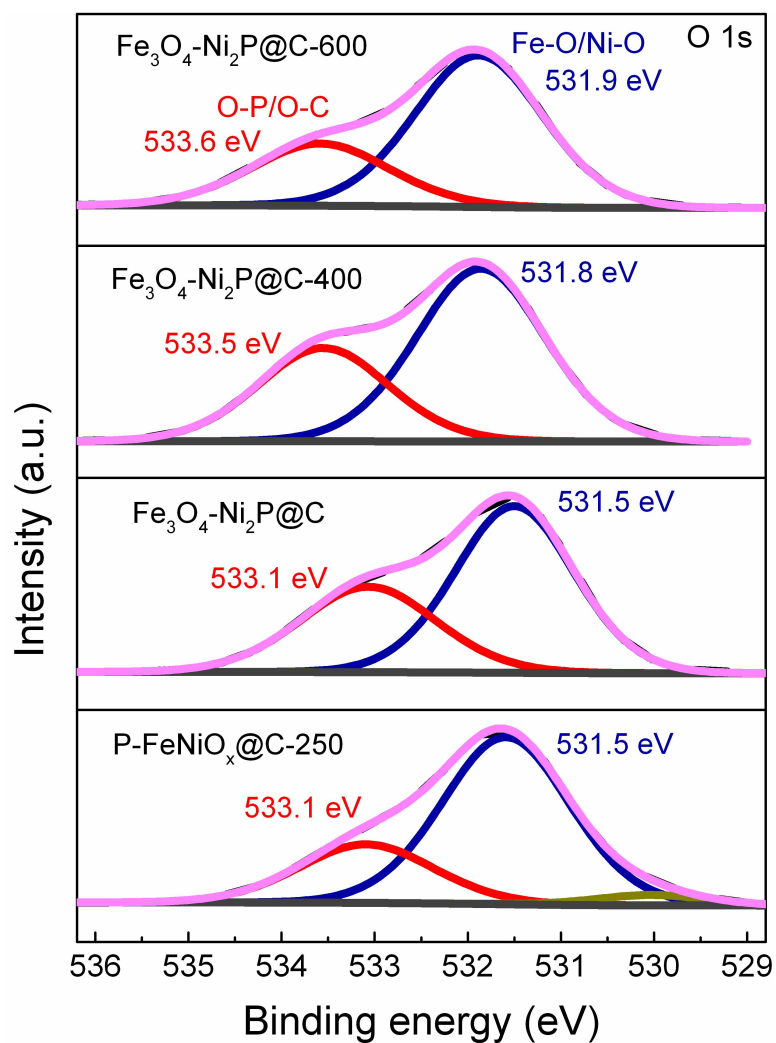
Fig. S12. High-resolution Ni 2p XPS spectra of samples prepared at different temperatures. In the Ni 2p spectra of samples prepared at different temperatures, the peaks at 856.7-857.2 and 874.6-875.2 eV could be ascribed to $2p_{3/2}$ and $2p_{1/2}$ orbitals of Ni^{2+} with the broad satellite peaks. Obviously, the peaks of Ni $2p_{3/2}$ and Ni $2p_{1/2}$ are shifted to higher binding energies with the increase in temperature. The peaks at 853.2-853.5 eV are linked to the formation of Ni-P. No Ni-P peak is observed in the Fe_3O_4-$Ni_2P@C$-250 sample, further verifying that the Ni_2P was generated at the phosphorization temperature above 300 °C.
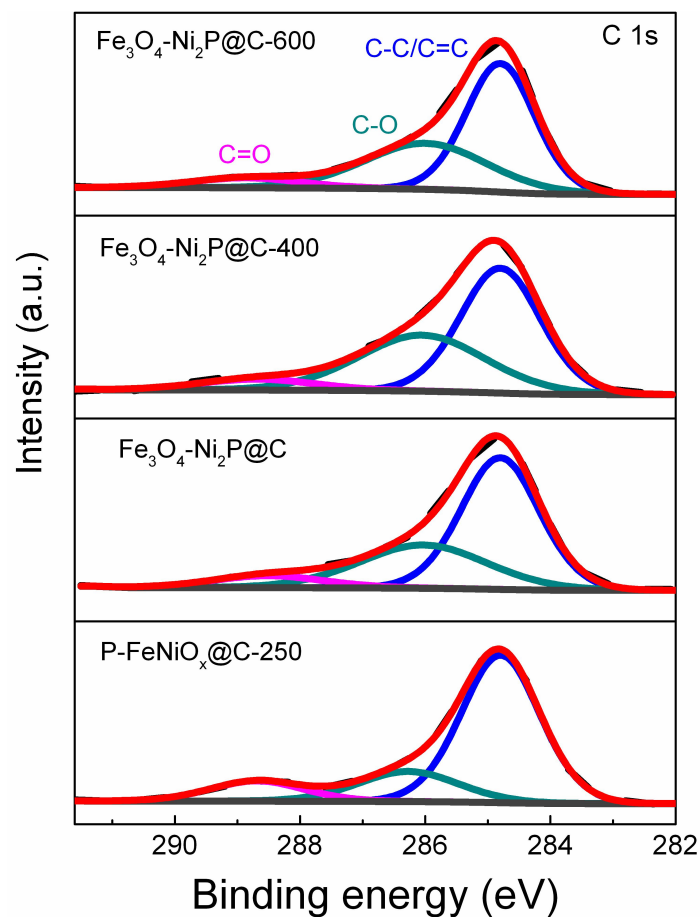
Fig. S13. High-resolution Fe 2p XPS spectra of samples prepared at different temperatures. In the Fe 2p spectra, the peaks at 710.1-710.6 and 711.5-715.2 eV could be assigned to Fe $2p_{3/2}$ orbitals of Fe^{2+} and Fe^{3+} with the satellite peaks, respectively. With the increase in temperature, the peaks of Fe $2p_{3/2}$ in Fe_3O_4-Ni_2P@C-400 and Fe_3O_4-Ni_2P@C-600 are shifted to lower binding energies. No Fe-P signal is observed even at high temperatures, indicating that no iron phosphide is generated in the bimetallic samples.

Fig. S14. High-resolution P 2p XPS spectra of samples prepared at different temperatures. The characteristic peaks at about 129.8 and 130.6 eV, corresponding to the P $2p_{3/2}$ and $2p_{1/2}$ states of metal phosphide, are also observed in the P 2p spectra of samples, except for the P-FeNiO$_x$@C-250 sample. This is consistent with the Ni 2p spectra. The broad peaks at 133.8-134.4 eV are attributed to the P-O species, which are shifted to higher binding energies with the increase in temperature.

Fig. S15. High-resolution O 1s XPS spectra of samples prepared at different temperatures. The peaks at 531.5-531.9 and 533.1-533.6 eV are characteristic of Fe-O/Ni-O and O-P/O-C groups, and these two peaks in the Fe_3O_4-Ni_2P@C-400 and Fe_3O_4-Ni_2P@C-600 samples are shifted to higher binding energies with the increase in temperature.

Fig. S16. High-resolution C 1s XPS spectra of samples prepared at different temperatures. The peaks at about 284.7, 286.1 and 288.7 eV are ascribed to C-C/C=C, C-O, and C=O groups, and no obvious shift is observed with the increase in temperature.
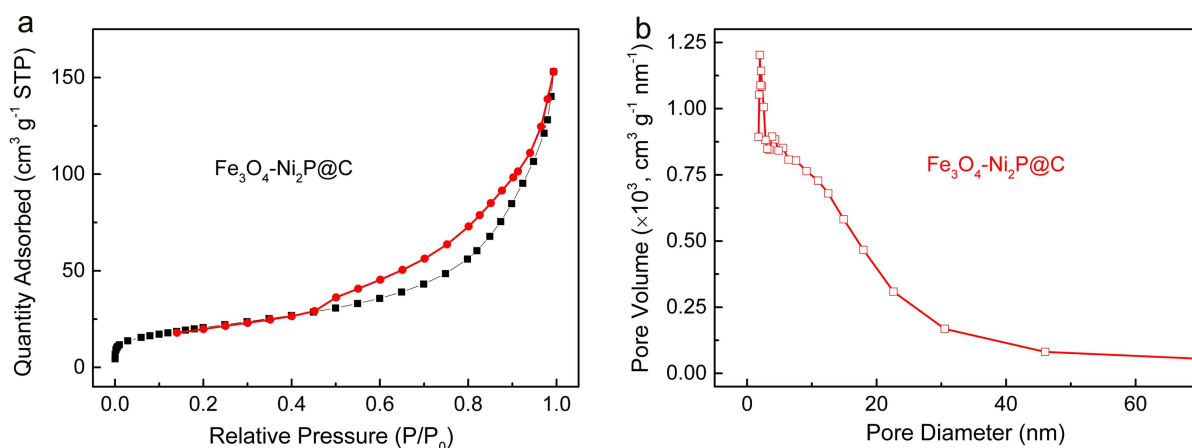

Fig. S17. (a) The N_2 adsorption-desorption isotherms and (b) pore-size distributions of Fe_3O_4-$Ni_2P@C$.
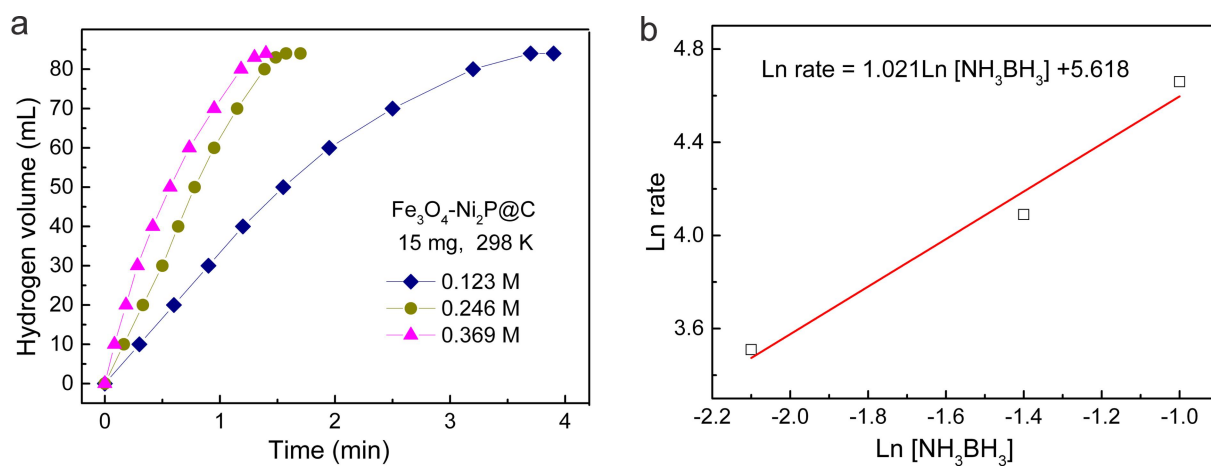
Fig. S18. (a) Hydrogen evolution for NH_3BH_3 hydrolysis at various NH_3BH_3 concentrations. (b) Logarithmic plots of rate versus concentrate of $[NH_3BH_3]$.
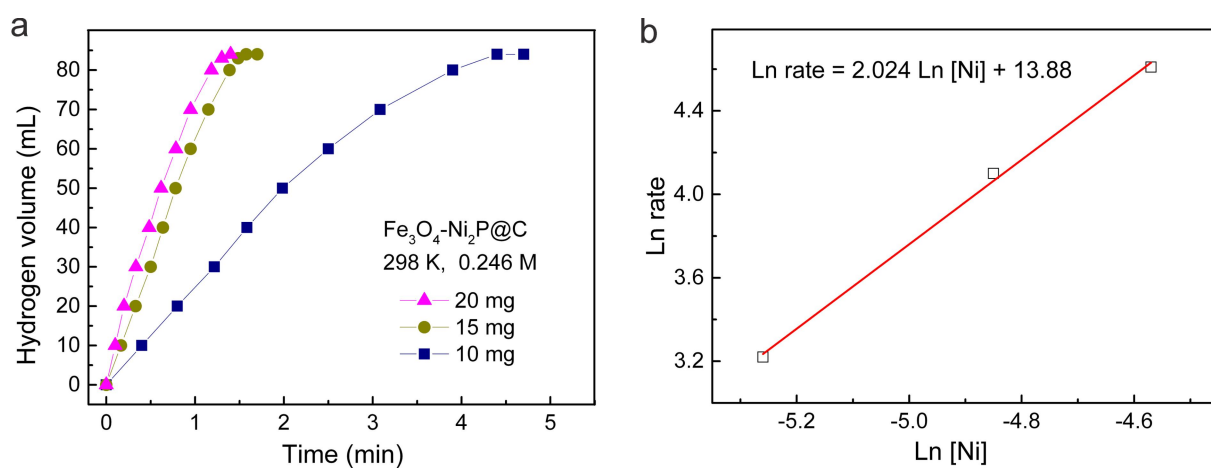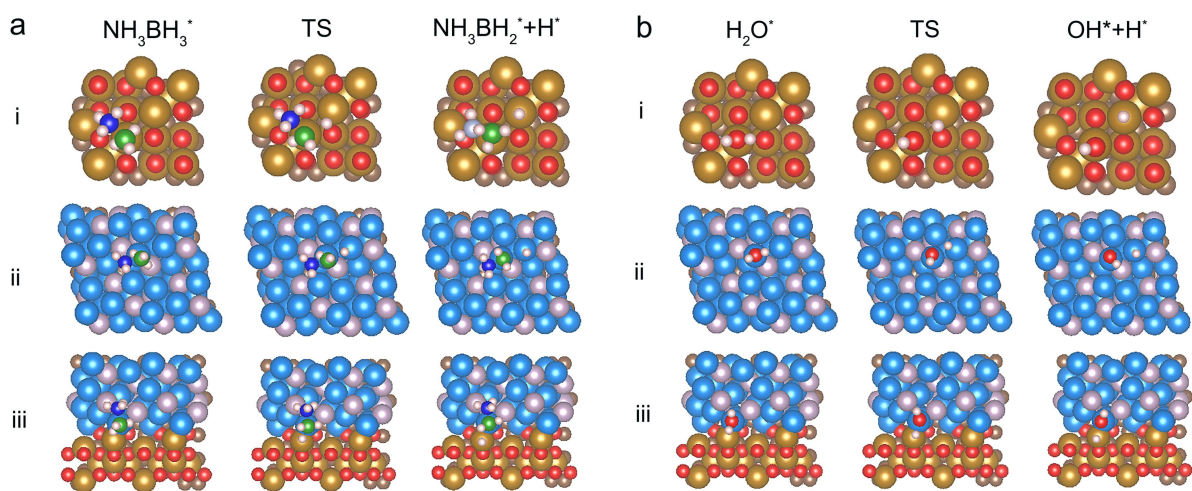

Fig. S19. (a) Hydrogen evolution for NH_3BH_3 hydrolysis at various catalyst amounts. (b) Logarithmic plots of rate versus concentrate of $[Ni]$.
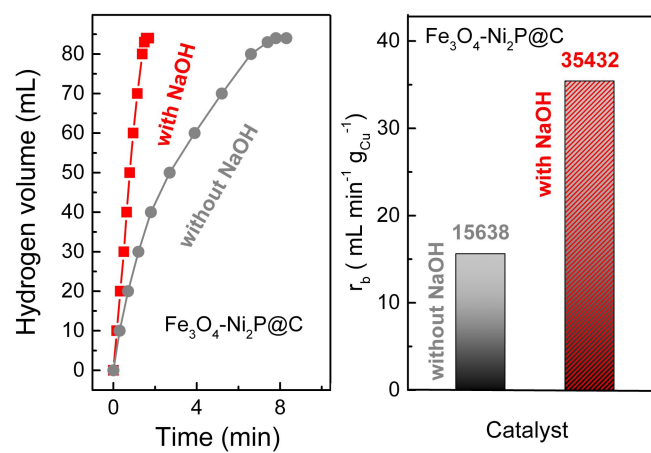
Fig. S20. Hydrogen generation for the NH₃BH₃ hydrolysis with 1.0 M NaOH and without NaOH at 298 K and corresponding rates values.
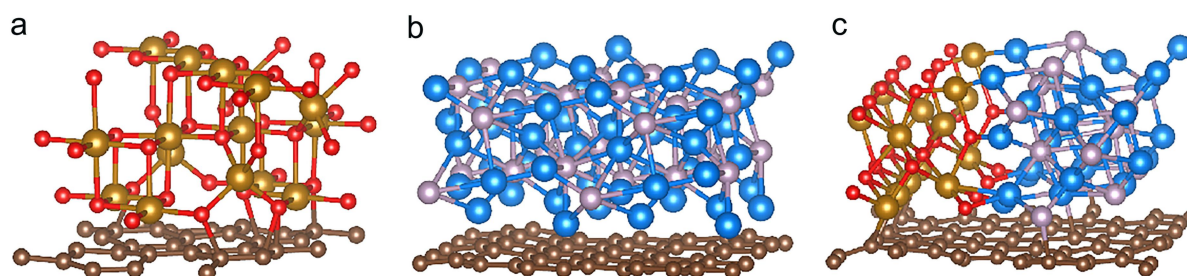
Fig. S21. The simulated structural models of (a) Fe₃O₄@C, (b) Ni₂P@C, and (c) Fe₃O₄-Ni₂P@C catalysts.

Fig. S22. i-iii are the optimized 3D structural models of (a) NH_3BH_3 and (b) H_2O adsorption and dissociation at $Fe_3O_4@C$, $Ni_2P@C$ and $Fe_3O_4-Ni_2P@C$ catalysts, respectively.

References

[1] G. Kresse, J. Furthmüller, Comp. Mater. Sci. 6 (1996) 15-50.

[2] G. Kresse, J. Furthmüller, Phys. Rev. B 54 (1996) 11169-11186.

[3] J.P. Perdew, K. Burke, M. Ernzerhof, Phys. Rev. Lett. 77 (1996) 3865-3868.

[4] G. Kresse, D. Joubert, Phys. Rev. B 59 (1999) 1758-1775.

[5] P.E. Blöchl, Phys. Rev. B 50 (1994) 17953-17979.

[6] C. Wang, J. Tuninetti, Z. Wang, C. Zhang, R. Ciganda, L. Salmon, S. Moya, J. Ruiz, D. Astruc, J. Am. Chem. Soc. 139 (2017) 11610-11615.

[7] W.J. Xu, M, Liu, S.F. Wang, Z.K. Peng, R.F. Shen, B.J. Li, Int. J. Hydrogen Energy 47 (2022) 23213-23220.

[8] A. Abutaleb, N. Zouli, M.M. El-Halwany, M. Ubaidullah, A. Yousef, Int. J. Hydrogen Energy 46 (2021) 35248-35260.

[9] H. Yen, Y. Seo, S. Kaliaguine, F. Kleitz, ACS Catal. 5 (2015) 5505-5511.

[10] M. Mahyari, A. Shaabani, J. Mater. Chem. A 2 (2014) 16652-16659.

[11] C.Y. Peng, L. Kang, S. Cao, Y. Chen, Z.S. Lin, W.F. Fu, Angew. Chem. Int. Ed. 54 (2015) 15725-15729.

[12] P.Z. Li, A. Aijaz, Q. Xu, Angew. Chem. Int. Ed. 51 (2012) 6753.

[13] J.K. Zhang, C.Q. Chen, W.J. Yan, F.F. Duan, B. Zhang, Z. Gao, Y. Qin, Catal. Sci. Technol. 6 (2016) 2112-2119.

[14] G.Q. Zhao, J. Zhong, J. Wang, T.K. Sham, X.H. Sun, S.T. Lee, Nanoscale 7 (2015) 9715-9722.

[15] S. Ghosh, S.R. Kadam, L. Houben, R. Bar-Ziv, M. Bar-Sadan, Appl. Mater. Today 20 (2020) 100693.

[16] P. Li, R. Chen, Y. Huang, W. Li, S. Zhao, S. Tian, Appl. Cataly. B: Environ. 300 (2022) 120725.

[17] P.Z. Li, K. Aranishiab, Q. Xu, Chem. Commun. 48 (2012) 3173.

[18] R.M. Brooks, I.M. Maafa, A.M. Al-Enizi, M.M. El-Halwany, M. Ubaidullah, A. Yousef, Nanomaterials, 9 (2019) 1082.

[19] S. Akbayrak, Z. Ozçifçi, A. Tabak, Biomass Bioenergy 138 (2020) 105589.

[20] H. Jiang, Y. Lin, B. Chen, Y. Zhang, H. Liu, X. Duan, D. Chen, L. Song, Mater. Today 21 (2018) 602-610.

[21] H. Chen, S. He, M. Xu, M. Wei, D.G. Evans, X. Duan, ACS Catal. 7 (2017) 2735-2743.

[22] Q. Hu, X.W. Huang, Z.Y. Wang, G.M. Li, Z. Han, H.P. Yang, X.Z. Ren, Q.L. Zhang, J.H. Liu, C.X. He, J. Mater. Chem. A 8 (2020) 2140-2146.